PHOTONICS Research

Orbital angular momentum beams demultiplexing using a hybrid Fourier phase shift neural network

Jiachi Ye,[1,†] Tongyao Wu,[1,†] Abdulaziz Bazammul,[1,†] Qian Cai,[1] Belal Jahannia,[1] Zibo Hu,[2] Hao Wang,[1] Hamed Dalir,[1,3] and Elham Heidari[1,*]

[1]Department of Electrical and Computer Engineering, University of Florida, Gainesville, Florida 32611, USA
[2]Fluctuology Inc., Arlington, Virginia 22207, USA
[3]Florida Semiconductor Institute, University of Florida, Gainesville, Florida 32611, USA
[†]These authors contributed equally to this work.
*Corresponding author: el.heidari@ufl.edu

Received 23 June 2025; revised 21 September 2025; accepted 25 September 2025; posted 1 October 2025 (Doc. ID 571526); published 1 December 2025

The exponential growth in data traffic has driven significant research into maximizing the capacity of free-space optical (FSO) communication systems. Orbital angular momentum (OAM) multiplexing offers a promising approach by using spatially structured beams with helical wavefronts to achieve higher data transmission rates. However, conventional electronic convolutional-neural-network-based OAM demultiplexing schemes exhibit substantial computational and energy efficiency limitations. In this paper, we introduce a hybrid optical-electronic Fourier phase shift neural network that implements phase-only feature extraction of the input multiplexed OAM beams in the Fourier domain. The proposed hybrid neural network uses phase spatial frequency kernels with the spatial light modulator to perform additive phase modulation of the Fourier-transformed input beams. Experimental results show that the proposed phase shift neural network has 6.5 times faster training time and three orders of magnitude higher energy efficiency compared to the designed conventional all-electronic convolutional neural network with one single convolution layer. The proposed system represents an idea towards energy-efficient, high-throughput optical neural networks for OAM-based FSO communication systems.

https://doi.org/10.1364/PRJ.571526

1. INTRODUCTION

The rapid increase in data results in a significant rise in worldwide network traffic, driven by bandwidth-demanding applications such as high-resolution video streaming, immersive virtual reality, cloud computing, and Internet of Things devices. The exponential growth in data needs has pushed conventional wireless communication technologies to their limitations, with existing systems facing substantial bandwidth constraints, energy efficiency, and latency requirements [1–4]. Free-space optical (FSO) communication offers advantages from the visible to near-infrared optical spectrum, offering significantly larger bandwidth than radio frequency systems. FSO communication uses light propagation in free space, avoiding physical transmission media, enabling high-capacity data networks with immunity to electromagnetic interference, improved security, and operation without licensing requirements [5–8]. These characteristics make FSO communication an appropriate option for addressing next-generation communication demands, especially when deploying conventional fiber-optic infrastructure faces logistical or financial challenges.

Among the various degrees of freedom explored for enhancing the capacity of FSO communication systems, orbital angular momentum (OAM) multiplexing was discovered as a promising method. Since Allen *et al.* [9] in 1992 established that light beams carrying OAM possess helical wavefronts with phase term $\exp(il\theta)$, where l is the topological charge and θ is the azimuthal angle, researchers have recognized the significant potential of OAM for multiplexing applications. The inherent orthogonality of OAM modes allows multiple data channels to co-propagate with minimal interference, theoretically enabling an ideally infinite number of topological charge states [10–12]. This property enables OAM multiplexing, which is particularly useful for FSO communication since it significantly improves data transmission capacity without increasing bandwidth needs. Structured light carrying OAM has drawn significant attention in communications and for various applications, including optical manipulation [13], high-resolution imaging [14–16], quantum information processing [17–21], and microscopy [22–24]. Traditional approaches for OAM demultiplexing have primarily depended on optical sorting

techniques, such as interferometric methods [25], diffractive optical elements [26], and mode sorters utilizing optical transformations [27]. These methods typically rely on the direct mapping of OAM states to spatial locations using conversion optics that convert helical wavefronts into plane waves. While effective under ideal circumstances, these traditional methods still face substantial implementation challenges, such as the necessity for bulky optical setups, precise alignment with subwavelength accuracy, and costly specialized optical components [28,29].

Researchers have explored computational approaches to address these limitations, particularly machine-learning-based image recognition techniques, which offer promising alternatives for OAM demultiplexing. These computational methods use the unique intensity patterns among different multiplexed OAM beams to identify and classify modes without requiring complex optical transformations. Machine learning approaches offer several advantages over traditional optical sorters, including enhanced robustness to noise and distortions, adaptability to varying channel conditions, and potential for more compact implementation without the strict alignment requirements of conventional systems [30]. Machine learning techniques, particularly convolutional neural networks (CNNs), have demonstrated promising capabilities for OAM demultiplexing under various conditions [31–36]. In standard convolutional neural network (CNN) architectures such as AlexNet, VGGNet, and GoogleNet, convolutional layers consume over 80% of the total runtime [37]. This computational workload results in substantial power consumption, thermal control challenges, and processing latency, especially concerning high-throughput OAM communication systems requiring real-time processing. Furthermore, phase-based optical processing offers distinct computational advantages over amplitude-based approaches. While amplitude-based systems require intensity modulation that inherently discards phase information, phase-only modulation preserves the complete optical field information during processing. This preservation becomes particularly significant when considering the computational efficiency of Fourier transform operations in the optical domain. As the number of OAM modes increases to leverage the advantages of multiplexing, computing demands correspondingly increase, creating a fundamental bottleneck in purely electronic implementations. These limitations highlight the need for alternative computing paradigms to maintain the classification accuracy of CNNs while significantly reducing their energy and processing time requirements for OAM demultiplexing applications. Optical computing has arisen as a viable method to address the computational constraints of electronic neural networks for OAM processing.

The 4f optical system is based on Fourier optics and enables convolution computing operations in the frequency domain by taking advantage of the intrinsic parallelism of light propagation [38,39]. In this 4f system, convolution between an input image and a kernel is realized by performing pixel-wise multiplication of their Fourier transforms in the Fourier domain, followed by an inverse Fourier transform. Chen [40] demonstrated an early implementation of optical matrix multiplication using a 4f system with computer-generated holographic masks at the Fourier plane. Modern implementations have advanced by replacing static holograms with programmable digital micromirror devices (DMDs), allowing for reconfigurable operations. These hybrid optical-electronic neural networks leverage optical processing for computationally intensive convolution operations while maintaining electronic processing for non-linear functions and weight updates. While the amplitude-based hybrid approaches represent significant progress, the inherent nature of OAM beams suggests that phase-only filtering methods may offer superior performance for OAM demultiplexing applications, where OAM beams fundamentally encode information in their helical phase structures, characterized by the $\exp(il\theta)$ phase factor that defines their topological charge. Fan *et al.* [41] explored complex-valued modulation methods for optical neural networks using a super-pixel approach with liquid-crystal-on-silicon spatial light modulators (LCOS-SLMs), demonstrating that phase information contributes to classification performance. A comprehensive investigation of phase-only filtering neural networks specifically optimized for OAM demultiplexing remains limited, creating a significant research opportunity at the intersection of optical computing and structured light processing.

In this study, we propose a hybrid Fourier optics phase shift neural network (PSNN) that implements phase-only feature extraction for OAM-coded signals demultiplexing in FSO communication systems. Unlike amplitude-based convolution approaches that process intensity information, the proposed system exploits the inherent phase structure of OAM beams using phase-only spatial frequency kernels with SLM through additive phase modulation in the Fourier domain. This approach aligns with the fundamental physics of OAM beams, where information is encoded in the helical phase factor $\exp(il\theta)$, potentially enabling more efficient optical computation. The proposed hybrid optical-electronic system performs optical computing through phase manipulation in the Fourier plane of a 4f optical system, followed by the rest of the electronic processing for training and recognition/demultiplexing. By performing convolutional feature extraction optically in the Fourier plane with programmable phase-only kernels, PSNN achieves low-power, phase-sensitive parallel processing. It also maintains the reconfigurability, the nonlinearity, and the adaptive training capabilities for electronic back-ends. This integration in two domains helps bridge the gaps in energy efficiency, adaptability, and scalability that neither all-electronic nor all-optical methods can fully solve on their own.

2. RESULTS AND DISCUSSION

A. Experimental Implementation

The proposed feature extraction of the OAM-coded bit string using a hybrid optical-electronic PSNN is depicted in Fig. 1. A fiber-coupled Fabry–Perot laser diode with 1550 nm wavelength is used as the beam source. The output beam is collimated and expanded to a diameter of 1.5 mm using a zoom fiber collimator and a beam expander to ensure enough coverage of the SLM active area. The beam passes through a linear polarizer, which is caged onto the beam splitter mount, oriented to maximize the phase modulation efficiency of the SLM. The expanded Gaussian-like beam is incident on the first

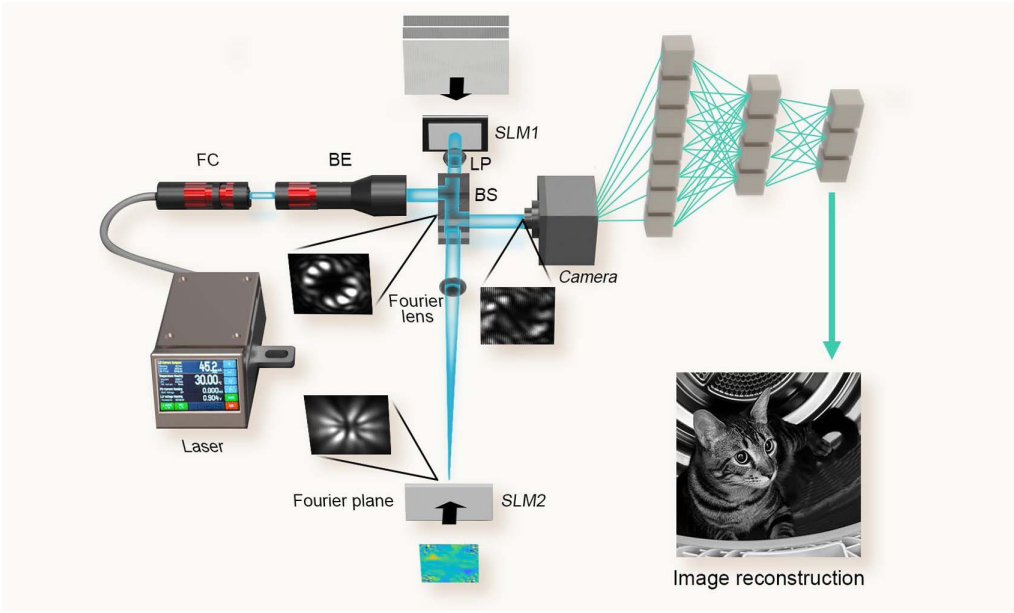

Fig. 1. Schematic diagram of orbital angular momentum (OAM) demultiplexing using Fourier optics phase shift neural network (PSNN) and image reconstruction using OAM shift keying (OAM-SK). The collimated Gaussian-like beam is converted into the LG mode via phase modulation using the spatial light modulator (SLM). Combined fork dislocation patterns are uploaded to generate the multiplexed OAM beams as bit-string signals. The Fourier lens performs the natural Fourier transform of the input OAM-coded signal according to the Huygens–Fresnel principle. The pre-trained phase spatial frequency kernels realize the feature extraction by the phase modulation with the input beam. The modulated beam is captured by the camera as electronic data to complete the rest of the neural network training electronically. Testing image is encoded and transferred using OAM-SK; the trained neural network model is used for OAM-coded signal recognition/demultiplexing and reconstruction. FC: fiber coupler; BE: beam expander; BS: beam splitter; LP: linear polarizer; SLM: spatial light modulator.

SLM (SLM1), which is programmed with computer-generated combined fork phase grating patterns designed to generate multiplexed OAM beams with predefined topological charges. For our 4-bit OAM-SK modulation scheme, we use four OAM modes with topological charges $l = -4$, 3, 5, and 7 to ensure sufficient separation between charge values and to implement appropriate Gouy phase differences, resulting in more distinguishable intensity patterns while minimizing potential intermode crosstalk that commonly occurs between adjacent topological charge values. It is important to note that this specific mode selection represents one optimized configuration for our demonstration. While our camera detection system can capture individual OAM modes within the range of $|l| \leq 10$ before beam expansion exceeds the sensor area, not all combinations within this range produce distinguishable multiplexed patterns. The interference between OAM modes generates intensity patterns determined primarily by mode spacing ($|l_2 - l_1|$) rather than absolute topological charge values, creating classification ambiguities when multiple combinations share identical spacing (see Visualization 1). Therefore, successful implementation requires careful pre-selection of OAM modes that generate unique interference patterns across all 16 possible combinations, as achieved with our chosen set of $l = -4$, 3, 5, and 7. Four multiplexed OAM modes create a dataset with 16 classes, each representing a 4-bit signal ranging from [0000] to [1111].

The SLM1 is fine-tipped/tilted to reflect the desired first diffraction order vertically back to the original path. The additional gradient phase term $k_x x$ ensures angular separation of diffraction orders, and with $k_x = 700$ rad/mm, the first-order beam is separated by ~2.6 cm at the detection plane ($f = 150$ mm). This large separation naturally isolates the desired order without requiring a 4f filtering system. The generated OAM-coded bit string then propagates through a biconvex Fourier lens with the focal length $f = 150$ mm, performing optical Fourier transformation of the input. At the back focal plane of the Fourier lens, the second SLM (SLM2) is placed and uploaded with 16 pre-trained phase spatial frequency kernels, realizing the feature extraction of the input Fourier-transformed OAM-coded bit strings. After being phase modulated by SLM2, the output is reflected through the Fourier lens, completing the inverse Fourier transform that converts the frequency-domain modulated information back to the spatial domain. A beam splitter then directs the modulated beam to the camera that captures the featured extracted intensity patterns as input for electronic processing, which includes a max-pooling layer (4×4) followed by two fully connected layers with 256 neurons (using ReLU activation) and a classification layer with 16 neurons corresponding to our 16 OAM-coded bit strings.

B. Generation of Multiplexed OAM Beams

In this study, we use the reflective phase-only SLM uploaded with phase-modulated fork grating patterns to convert the input Gaussian-like beam to the Laguerre–Gaussian (LG) modes. The fork dislocation patterns uploaded on the SLM are eight-level grayscale images calculated by

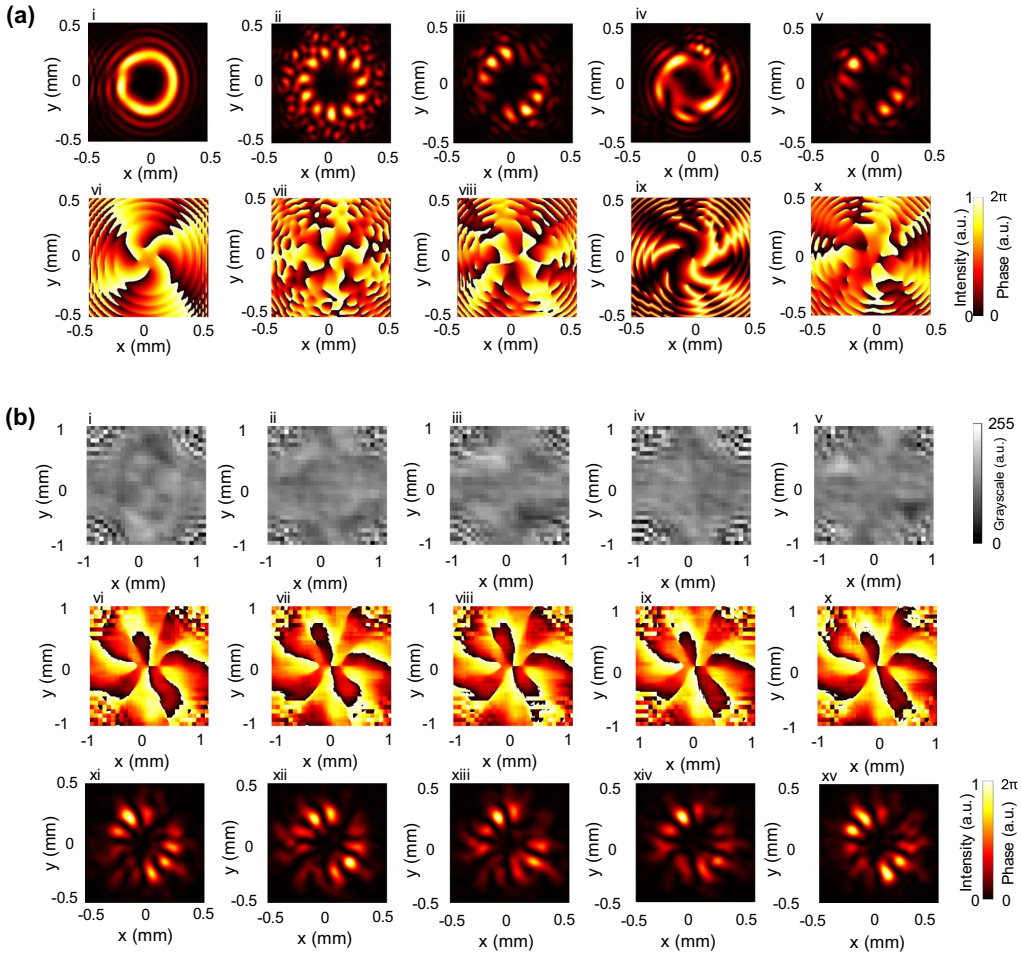

Fig. 2. Example demonstration of phase modulation and feature extraction of multiplexed orbital angular momentum (OAM) beams. (a) Intensity (i–v) and phase (vi–x) profiles of the generated multiplexed OAM beams. These beams are generated by having a Gaussian beam modulated by the phase fork dislocation patterns. The corresponding topological numbers (from left to right) are $l = -4$ (i, vi); $l = -4$, 7 (ii, vii); $l = -4$, 5, 7 (iii, viii); $l = 3$, 5, 7 (iv, ix); and $l = -4$, 3, 5, 7 (v, x), respectively. The ripples in the intensity and phase patterns come from the contributions of higher radial order ($p \neq 0$) modes. The rotational feature originates from the Gouy phase term in the LG mode expression Eq. (3) when $z \neq 0$. These simulated results show the characteristics of the practical generated multiplexed OAM beams and serve as the fundamental data for phase spatial frequency kernels training. (b) Examples (using multiplexed OAM signal $l = -4$, 5, 7) of the pre-trained phase spatial frequency kernels (i–v), which are loaded on the second spatial light modulator (SLM2), phase distribution of the multiplexed OAM-coded signals after being phase modulated by the phase kernels (vi–x), and intensity distribution of feature-extracted output after inverse Fourier transform (xi–xv), respectively.

$$I_l = \frac{1}{2}[1 + \cos(k_x x + l\theta)], \tag{1}$$

whose grayscale at each pixel corresponds to a phase shift between 0 and 2π. We generate the multiplexed OAM beams by combining the fork grating patterns of n different topological numbers l together: $I = \frac{1}{n}\sum_l I_l$. Examples of the intensity and phase profiles are shown in Figs. 2(a)(i)–2(a)(v) and 2(a)(vi)–2(a)(x), respectively, where topological numbers $l = -4$, 3, 5, and 7 are used to generate OAM-multiplexed beams.

C. Phase-Only Feature Extraction

Traditional feature extraction and image recognition are conducted on an amplitude-only 2D image without phase information. Unlike amplitude-only images, the light field is a vector field consisting of amplitudes, directions, and phases. Here, we perform the phase-only feature extraction using the pre-trained phase spatial frequency kernels. Unlike conventional electrical convolutional neural networks, our approach applies the Fourier transformation and kernel feature extraction within an optical Fourier domain process. A Fourier lens with a focal length of $f = 150$ mm is used, effectively performing a Fourier transform on the incoming light field, which is projected onto SLM2 for further processing. We place the lens at its focal distance away from SLM1 on the beam path of the first diffraction order and put SLM2 at the back focal plane. Assuming the paraxial conditions and the OAM-multiplexed light field is $u_1(x, y)$ at the SLM1 plane, the field on SLM2, according to the Huygens–Fresnel principle [42], will be

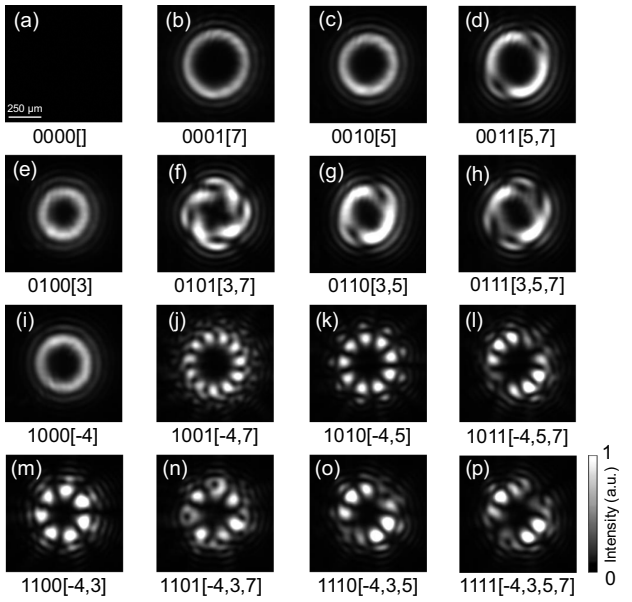

Fig. 3. Experimentally generated intensity profile of 4-bit orbital angular momentum (OAM)-coded signal. (a)–(p) OAM-coded 4-bit string ranging from [0000] to [1111] where the selective OAM modes are active, serving as the OAM shift keying (OAM-SK) signal used for testing image encoding and transferring. A gray-scale color bar and a scale bar of length 250 μm are drawn.

$$u_2(x_2,y_2) \approx \exp\left[i\pi\frac{x_2^2+y_2^2}{\lambda f}\left(1-\frac{z}{f}\right)\right]\cdot G\left(\frac{x_2}{\lambda f},\frac{y_2}{\lambda f}\right). \quad (2)$$

Here (x_1,y_1) and (x_2,y_2) are the coordinates on the SLM1 plane and the focal plane, and $\lambda = 1550$ nm is the wavelength. $G_1(k_x,k_y) = u_1(x,y)\iint \exp[i2\pi(xk_x+yk_y)]\mathrm{d}x\mathrm{d}y$ is the Fourier transform of the light field from SLM1. Therefore, the field on SLM2 is essentially the Fourier transform of u_1, and the momentum spatial phase kernel feature extraction is passively completed when the light is reflected from SLM2. Inverse Fourier transform is done by the backtrace of light through the Fourier lens, as the feature-extracted output shown in Figs. 2(b)(xi)–2(b)(xv). This phase-only feature extraction, which is realized by optical Fourier transform and physical phase modulation, is both time- and energy-saving compared to the electrical computation.

D. Neural Network System Performance

We use the combined fork dislocation phase patterns uploaded onto the SLM to generate the multiplexed OAM beams, as intensity profile shown in Fig. 3. Each multiplexed OAM pattern represents the OAM-coded 4-bit string from [0000] to [1111], where the selective OAM modes are active. The proposed PSNN includes the phase modulation layer, where we realized the feature extraction of the input OAM-coded signal in the Fourier domain; after the inverse Fourier transform via the reflection from SLM2 and being directed by the beam splitter, the transformed output is captured by the camera and collected as the dataset used for training. For each class of 16 4-bit-string OAM-coded signals, 500 input images are generated by SLM1 using designed fork-grating patterns for training and testing. SLM2 sequentially uploads 16 pre-trained phase-frequency kernels for each class, yielding 8000 outputs per class. In total, 128,000 outputs across 16 classes are used to form the training and validation sets with a split ratio of 8:2. The dataset is grouped in sets of 16 and pre-processed with random shuffling and rotation to enhance the dataset variety. The neural network training was implemented using the TensorFlow software framework with GPU acceleration enabled on an NVIDIA GeForce RTX 4080 graphics processing unit. The rest of the neural network consists of a flattened layer and two fully connected layers using the ReLU activation function and the softmax activation function with 16 neurons. To test and analyze the proposed PSNN performance, we run the dataset training on a designed conventional all-electronic convolutional neural network (ECNN) with one convolution layer and compare the classification accuracy of PSNN with ECNN, where we define the demultiplexing accuracy as the classification accuracy of both neural networks based on OAM-coded signals' unique intensity patterns. We run both neural networks over 50 epochs five times, and the averaged results are shown in Fig. 4, with shaded regions representing variability across five independent training runs. The comprehensive training results are shown in Table 1. The ECNN model achieved a final

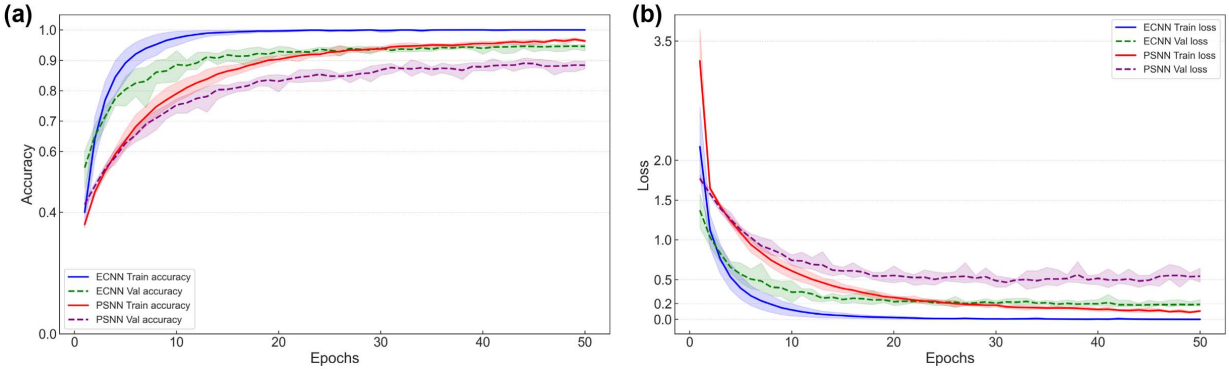

Fig. 4. Trained models' performance for 4-bit orbital angular momentum (OAM)-coded signal recognition/demultiplexing of all electronic convolutional neural network (ECNN) and phase shift neural network (PSNN). (a) Training and validation accuracy curves of ECNN (94.66% ± 0.49%) and PSNN (89.01% ± 1.08%). (b) Training and validation loss curves of ECNN and PSNN. The shaded area represents the range of min-max results of five runs.

Table 1. System Performance Comparison between the Electronic Convolutional Neural Network and the Phase Shift Neural Network

	Training Performance			Computational Efficiency		
Model	Best Val. Acc. (%)	Best Val. Loss	Final Val. Loss	FLOPs (million)	Training Time (s/epoch)	Energy Eff. (GOPS/W)
ECNN	94.66 ± 0.49	0.18 ± 0.01	0.19 ± 0.03	36.64	235.40	6.9×10^{-7}
PSNN	89.01 ± 1.08	0.47 ± 0.04	0.54 ± 0.06	112.86	36.26	1.23×10^{-3}

validation accuracy of $94.58\% \pm 0.77\%$ after 50 epochs, with the highest validation accuracy of $94.66\% \pm 0.49\%$ at epoch 49, with an average full training time of 11,770.15 s. The proposed PSNN model showed a final validation accuracy of $88.37\% \pm 0.87\%$ and highest validation performance of $89.01\% \pm 1.08\%$ at epoch 44, with an average full training time of 1812.79 s.

Although the PSNN's accuracy of 89.01% trails the ECNN's 94.66% by 5.7%, this performance gap directly reflects our designed choice to constrain both networks to single convolutional layers, enabling fair comparison of the optical versus electronic processing modalities rather than pursuing maximum absolute performance through deeper architectures. This accuracy difference fundamentally stems from the inherent trade-offs in phase-only optical processing, where complex weights are restricted to unit magnitude $e^{i\phi}$, compared to the freely tunable real-valued weights that provide greater optimization flexibility in electronic implementations. This comparison was structured with both networks implementing single convolutional layers to ensure architectural parity and enable direct evaluation of optical versus electronic processing for the convolution operation. The ECNN was designed to avoid multiple layers or complex architectures to maintain a fair comparison with what can be practically implemented in our current optical hardware—a single Fourier transform with phase kernel stage. While deeper electronic networks would achieve higher accuracy, such comparisons would obscure the fundamental assessment of optical acceleration benefits for the computationally intensive convolution operation, which constitutes approximately 48.65% of the total computational load in our single-layer ECNN and 84.26% in the PSNN.

Despite these constraints, the accuracy-efficiency trade-off demonstrates clear advantages for specific application scenarios. The 6.5-fold reduction in training time and three orders of magnitude improvement in energy efficiency make the PSNN particularly suitable for high-throughput applications where power consumption and processing speed are critical constraints. For many practical OAM communication systems, modern forward error correction codes can effectively compensate for the modest accuracy reduction while benefiting from the substantial improvements in throughput and power consumption.

To evaluate the robustness of our proposed PSNN under realistic atmospheric conditions, we conducted preliminary simulations incorporating weak turbulence effects, where we implemented the modified von Kármán atmospheric turbulence model for simulating OAM-coded signal experiencing weak atmospheric turbulence condition of $D/r_0 = 0.1$ (the simulated turbulence-affected OAM-coded signal is demonstrated in Visualization 2), where D represents the physical dimension of the SLM, and r_0 is the Fried parameter. We train the turbulence-effected OAM-coded signal for both neural networks. The validation results (shown in Visualization 3) demonstrate that the PSNN maintains superior resilience to turbulent conditions, with accuracy decreasing by only 1.87 percentage points (from 90.05% to 88.18%) compared to a 3.80 percentage point reduction for the ECNN (from 96.42% to 92.62%). This reduced sensitivity to turbulence-induced phase distortions empirically validates our hypothesis that phase-only processing naturally accommodates atmospheric perturbations more effectively than amplitude-based approaches.

E. Image Reconstruction

We built a 0.4 m OAM shift keying (OAM-SK) modulation FSO communication link to encode and transfer the 8-bit grayscale image using our 4-bit OAM-coded string dataset, where each pixel value of the test images is represented by two strings for high 4-bit and low 4-bit separately. Both trained neural network models, ECNN and PSNN, are used to decode and reconstruct the transferred images with different sizes, as shown in Fig. 5. The ECNN and PSNN models were tested to reconstruct the images five times. The averaged pixel error rate (PER) of the ECNN reconstructed image over five times is 2.59%, 2.30%, and 0.88% for the testing image pixel sizes 200×200, 300×300, and 400×400, respectively; the averaged PER of the PSNN reconstructed image over five times is 3.19%, 2.77%, and 1.37% for the testing image pixel sizes 200×200, 300×300, and 400×400, respectively. Two images with less pixel difference were also tested under the same configurations; for the testing image with less pixel difference [Fig. 6(a)], the averaged PER is 1.18%, 0.14%, 0.12%, and 3.69%, 2.75%, 1.08% [Fig. 6(c)] for the ECNN model and PSNN model with the image sizes 200×200, 300×300, and 400×400, respectively; for the testing image with the lowest pixel difference [Fig. 6(d)], the averaged PER is 0.86%, 0.69%, 0.02%, and 1.64%, 1.55%, 0.96% [Fig. 6(f)] for the ECNN model and PSNN model with the image sizes 200×200, 300×300, and 400×400, respectively. These reconstructed results, in which larger image sizes manifest superior reconstruction fidelity despite possessing more pixels susceptible to erroneous prediction, can be attributed to several information processing schemes. The higher information density in smaller images necessitates each pixel to encapsulate more of the original visual information, thereby increasing reconstruction complexity and error propensity. Furthermore,

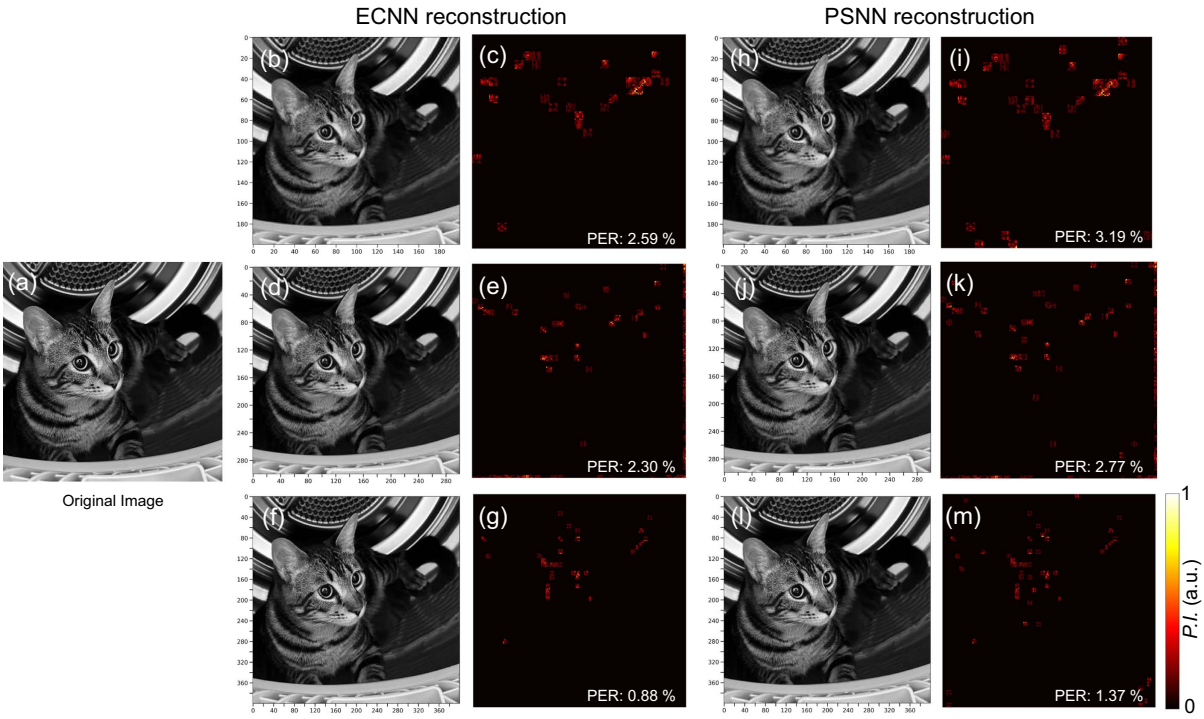

Fig. 5. Image reconstruction results using orbital angular momentum shift keying (OAM-SK) over a 0.4 m free-space optical communication link. (a) Original image used for encoding. The two columns in the middle show the reconstructed images using the trained electronic convolutional neural network (ECNN) model and the calculated pixel error rate (PER) results shown at the bottom-right corner of the color difference plots for the testing image sizes 200 × 200 (b), (c), 300 × 300 (d), (e), and 400 × 400 (f), (g); the two columns on the right show the reconstructed images using the trained phase shift neural network (PSNN) model and the calculated PER results with the color difference plots for the testing image sizes 200 × 200 (h), (i), 300 × 300 (j), (k), and 400 × 400 (l), (m). The color bar is normalized to [0,1] by dividing each absolute pixel difference value by the maximum pixel difference. P.I., pixel intensity.

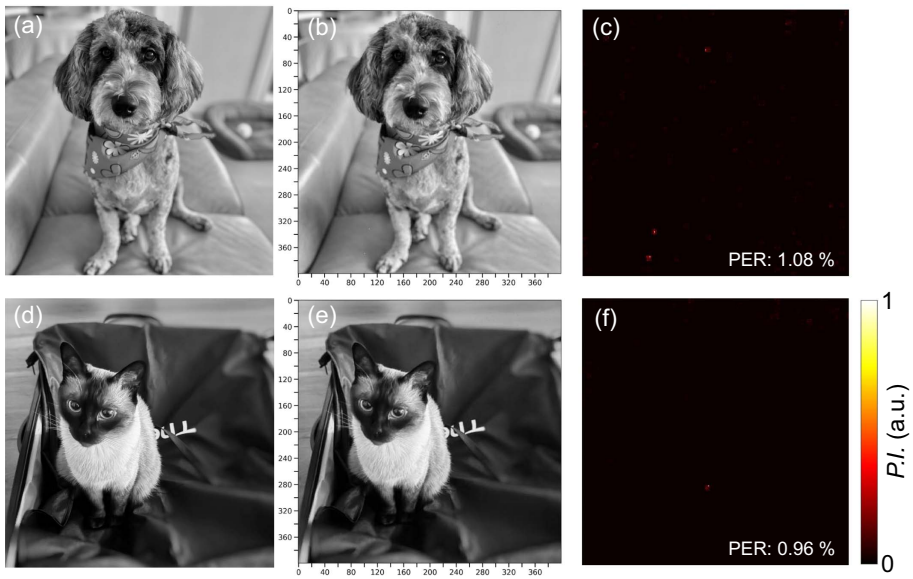

Fig. 6. Image reconstruction results for testing images with less pixel difference using orbital angular momentum shift keying (OAM-SK) over a 0.4 m free-space optical communication link. (a) Original testing image with less pixel difference compared with the first testing image. (b) The reconstructed image with the pixel size 400 × 400. (c) The pixel difference plot between the original testing image and the reconstructed image, with the calculated pixel error rate (PER) (1.08%) shown at the bottom-right corner. (d) Original testing image with the relatively lowest pixel difference. (e) The reconstructed image with the pixel size 400 × 400. (f) The pixel difference plot between the original testing image and the reconstructed image, with the calculated PER (0.96%) shown at the bottom-right corner. The color bar is normalized to [0,1] by dividing each absolute pixel difference value by the maximum pixel difference. P.I., pixel intensity.

larger images provide enhanced contextual information through increased pixel jointy, facilitating more accurate value predictions through spatial correlation advantages. Edge effects disproportionately impact smaller images, where boundary pixels constitute a higher proportion of the total pixel population. Additionally, the error propagation mechanisms appear to operate non-linearly with respect to image dimensionality, suggesting that reconstruction schemes from trained neural network models benefit from the redundancy and contextual richness inherent in higher-resolution representations.

F. Computational Efficiency

As detailed in the introduction of Section 4, the total number of floating point operations (FLOPs) of our designed ECNN $\text{FLOPs}_{\text{total}}$ is calculated as 36,638,576 FLOPs, with the convolution layer accounting for 17,825,792 FLOPs. Compared with complex neural network architectures, which have multiple convolutional layers with varying kernel sizes, our ECNN is designed with a single convolutional layer to align with the practical free-space optical implementation, followed by two dense layers. The convolutional layer accounts for approximately 48.65% of the total computational load. This validates the potential benefits of implementing optical acceleration methods for the convolutional components of neural networks. For the proposed PSNN, we have the total number of FLOPs $\text{FLOPs}_{\text{total}}$ as 112,856,944 FLOPs, where the optical component in the designed Fourier phase shift layer of the PSNN has 95,092,736 FLOPs, accounting for 84.26% of the total computational load. This result addresses the computational intensity of the Fourier transform operations, particularly the inverse FFT applied to multiple phase masks. The optical operations are performed in parallel through physical light propagation, enabling significantly faster processing despite the higher FLOPs count. The performance analysis reveals substantial improvements in processing speed and energy efficiency with the PSNN architecture. As shown in Table 1, the PSNN demonstrates a 6.5 times reduction in training time, highlighting the parallel processing advantage of the optical implementation. Most notably, the energy efficiency of the PSNN, measured in giga-operations per second per watt (GOPS/W), is 1.23×10^{-3} GOPS/W—approximately three orders of magnitude higher than the ECNN's efficiency of 6.9×10^{-7} GOPS/W. This improvement in energy efficiency contributes to the inherent parallelism of optical computations and the elimination of energy-intensive electronic components for the majority of the computational operations. This demonstrates the substantial potential of optical computation in high-throughput neural network processing, particularly for applications involving complex phase information that electronic systems struggle to process efficiently.

The proposed PSNN offers a unique balance when compared to both traditional optical methods and machine-learning-based OAM demultiplexing techniques. Purely optical methods such as interferometers, diffractive optical elements, and log-polar mode sorters provide real-time, parallel separation of modes with high fidelity under ideal conditions. The log-polar transformer [26] (two static plates and a lens) and its improvements [43] have reached experimental separation efficiencies over 92%. However, these systems are often fixed in hardware, sensitive to alignment, and not very flexible in response to changing channels or turbulence. In contrast, the PSNN maintains optical speed but replaces fixed optics with a learned, reconfigurable phase-only Fourier-plane kernel on a spatial light modulator (SLM). This kernel can be updated in software through retraining and can be taught to recognize patterns distorted by turbulence—something that fixed sorters cannot handle effectively. Compared to electronic or machine learning demultiplexers, CNN-based receivers usually report very high accuracies [44,45], but their heavy convolutional workloads, which often account for over 90% of operations, lead to latency and power limitations that become tighter as the mode count increases. The PSNN shifts the main convolution step to passive optical propagation through a 4f Fourier layer, which preserves phase information that amplitude-only optical filters lose. This approach leaves only lightweight electronic layers for classification. Together, the PSNN uniquely fills a gap: it is more compact and resilient than conventional optics, and it is significantly more energy-efficient and faster than all-electronic neural networks. This positions it as a strong candidate for scalable, high-capacity OAM-based free-space optical communication systems.

The selection of appropriate OAM mode combinations represents a fundamental design consideration for multiplexed OAM communication systems. As demonstrated in Visualization 1, closely spaced modes such as $l = 7, 8, 9, 10$ create overlapping pattern spaces where distinct bit strings become indistinguishable to the classification system. This physical constraint, arising from the interference properties of superimposed OAM beams, necessitates optimization algorithms for mode selection that maximize pattern distinguishability while maintaining desired channel capacity. Future work should explore systematic approaches for identifying optimal mode sets under various system constraints.

However, the current study still faces limitations. The phase-only approach introduces certain constraints on the complexity of feature extraction, potentially limiting the network's ability to capture subtle intensity variations compared to amplitude-based methods. Additionally, the current implementation relies on SLMs with operation frequency limited to 60 Hz, restricting the temporal throughput of the optical processing stage. Further optimization of the neural network architecture and system configuration could yield additional improvements in both accuracy and efficiency. Specifically, implementing both amplitude and phase modulation to realize the full complex Fourier transform and designing parallel multiplexed signals on SLM simultaneously for multi-output optical processing might enhance the network's feature extraction capabilities without increasing energy consumption. The energy efficiency improvements demonstrated by the proposed PSNN architecture have important implications for sustainable computing in data-intensive applications. As the volume of data transmitted through optical communication systems grows exponentially, the energy consumption associated with signal processing becomes increasingly critical. The OAM-involved hybrid neural network architecture offers an ideal approach towards more energy-efficient FSO communication systems, contributing to the broader goal of sustainable optical communication and computing development.

Atmospheric turbulence presents a fundamental challenge for OAM-based free-space optical communication, primarily manifesting as random phase fluctuations that distort the helical wavefront structure. However, our phase-only filtering approach offers distinct advantages in turbulent conditions compared to conventional amplitude-based processing. Since turbulence predominantly affects the phase component of optical fields while often preserving relative intensity distributions, amplitude-based systems that discard phase information lose critical data needed for turbulence compensation. In contrast, our PSNN directly processes and preserves this phase information, enabling the network to learn characteristic turbulence-induced phase patterns as distinguishable features rather than treating them as noise. The PSNN architecture transforms the turbulence challenge into a classification problem with learnable solutions. During training with turbulence-degraded datasets, the network develops phase kernels that capture invariant relationships between OAM modes even under distorted conditions. Our preliminary simulations provide quantitative support for this theoretical framework. Under weak turbulence conditions, the PSNN demonstrated approximately 50% less performance degradation compared to the ECNN, maintaining 88.18% accuracy versus 92.62% for the amplitude-based system. This differential resilience arises from the fundamental alignment between the phase-only processing domain and the primary manifestation of atmospheric turbulence as phase distortions. Building on these inherent advantages, our future development will focus on implementing advanced algorithmic turbulence compensation techniques that leverage the computational flexibility of the neural network architecture. This software-based approach eliminates the need for traditional hardware solutions such as adaptive optics systems with probe Gaussian beams, deformable mirrors, wavefront sensors, and complex servo control loops, which add substantial cost, complexity, and alignment challenges to FSO communication systems. By incorporating turbulence-adaptive algorithms directly into the phase kernel training process, we anticipate achieving comparable or superior compensation performance while maintaining the simplicity and cost-effectiveness of our passive optical implementation. The scalability to higher-order multiplexing presents both challenges and opportunities. As the number of OAM modes increases from four to N, the classification complexity grows exponentially (2^N classes), requiring expanded phase kernel sets and larger training datasets. However, our optical Fourier transformation maintains constant processing time regardless of mode count, whereas electronic convolution scales with $O(N^2)$ complexity. This fundamental difference suggests that the efficiency advantages of our approach will become more pronounced at higher multiplexing orders. Our current demonstration with 16 classes shows 6.5 times faster training projects to potentially 20-fold acceleration for 256 classes (eight-mode multiplexing) based on computational scaling analysis. Future implementations will incorporate adaptive training methodologies using synthetic turbulence models with varying strength parameters to develop robust classification strategies. The algorithmic approaches combined with the inherent phase-sensitivity of our architecture, provide a pathway toward practical deployment without requiring complex adaptive optics hardware.

3. CONCLUSIONS

In this study, we demonstrate the effectiveness of the proposed hybrid phase shift Fourier neural network for demultiplexing OAM beams. By implementing phase modulation in the Fourier domain, we realize the feature extraction of the input multiplexed OAM-coded signals, yielding advantages in computational efficiency while maintaining a demultiplexing accuracy of 89.01% compared to 94.66% for the ECNN model. The proposed PSNN demonstrates substantial improvements in both processing speed and energy efficiency. The training time for the PSNN was 6.5 times faster than the ECNN, highlighting the operational advantage conferred by optical implementation of the computationally intensive Fourier transform operations. This acceleration becomes significant when considering the processing requirements for real-time OAM-based communication systems, where rapid demultiplexing is essential for maintaining high data throughput. The inherent parallelism of optical processing enables the simultaneous execution of these operations with minimal energy expenditure, whereas conventional neural networks require energy-intensive electronic computations. The computational analysis also addresses the advantages of the hybrid neural network, particularly for applications involving phase-encoded information. While electronic neural networks excel at amplitude-based pattern recognition, they might face fundamental efficiency limitations when processing phase-encoded data that must be converted to amplitude representations. The proposed PSNN architecture demonstrates its computational advantages that extend beyond the immediate performance metrics. While the FLOPs count for the PSNN (112.86 million) exceeds that of conventional amplitude-based approaches due to the FFT operations, the optical implementation operating in the Fourier domain fundamentally transforms these computations. The Fourier transform operations, which constitute 84.26% of the total computational load in the proposed PSNN, are performed passively through optical propagation. This computational advantage becomes increasingly pronounced when considering system scalability. For larger OAM mode sets and higher data rates, the phase-based approach maintains constant processing time regardless of the computational complexity. In contrast, traditional electronic convolution implementations would experience linear or superlinear increases in processing time with system scale. This scalability characteristic positions phase modulation optical processing as a critical enabling technology for next-generation high-capacity optical communication systems. Preliminary simulations under weak atmospheric turbulence conditions further validate the phase-only approach, demonstrating reduced performance degradation compared to amplitude-based processing and supporting the theoretical advantages of operating directly in the phase domain where turbulence effects primarily manifest.

4. METHODS/EXPERIMENT

A. OAM and Mode Multiplexing

Light beams carrying OAM are characterized by their helical wavefront structure and are usually mathematically described as Laguerre–Gaussian (LG) beams with the radial index p and topological charge l. While the amplitude remains

rotationally symmetric, a nonzero topological charge determines the number of 2π phase shifts in one rotation around the beam axis, creating a distinctive phase singularity at the center of the beam. In cylindrical coordinates, an LG mode with wavevector k_0 can be written as [46]

$$\mathrm{LG}_p^l(r,\theta,z) = \sqrt{\frac{2p!}{\pi(p+|l|)!}}\left[\frac{r\sqrt{2}}{\omega(z)}\right]^{|l|} L_p^{|l|}\left[\frac{2r^2}{\omega^2(z)}\right] \times \frac{\omega_0}{\omega(z)} e^{-\mathrm{i}\phi_{pl}(z)} e^{-\frac{r^2}{\omega^2(z)}} e^{\mathrm{i}\frac{k_0 r^2}{2R(z)}} e^{\mathrm{i}l\theta}, \quad (3)$$

where r, θ, and z are the radial distance, azimuthal angle, and propagation distance, respectively. L_p^l is the generalized Laguerre polynomial. $\omega(z) = \omega_0[(z^2+z_R^2)/z_R^2]^{1/2}$ is the beam radius at a distance z away from the beam waist, with ω_0 being the radius of the beam waist and z_R the Rayleigh range. $\phi_{pl}(z) = (2p+|l|+1)\arctan(z/z_R)$ is the Gouy phase, which accumulates gradually as the wave propagates. LG modes with different p or l are orthogonal to each other, forming a complete and orthogonal basis of propagating light. In our experiments, we generate and use the single-ringed LG modes (LG_p^l) with radial index $p = 0$ (LG_0^l) to produce well-defined optical ring intensity patterns with optical clarity. When a collimated Gaussian beam $u(r,\theta,z) = U_0 \exp(-r^2/\omega_0^2)\exp(-\mathrm{i}k_0 z)$ is illuminated at the center of the SLM, the field right after reflection is

$$u_l(r,\theta,z) = U_0 e^{-r^2/\omega_0^2 + \mathrm{i}(2\pi I_l + k_0 z)}, \quad (4)$$

where I_l is the grayscale image of the fork grating pattern uploaded on SLM, as given in Eq. (1). Due to the periodic phase modulation, the field can be decomposed into orthogonal components propagating in different directions:

$$u_l(r,\theta,z) = \sum_{p,n} U_{p,nl}\mathrm{LG}_p^{nl}(r,\theta,z) e^{\mathrm{i}(nk_x x + k_0 z)}, \quad (5)$$

where $x = r\cos\theta$ and

$$U_{p,l} = U_0 \int_0^{2\pi}\int_0^{\infty} \sqrt{\frac{2p!}{\pi(p+|l|)!}}\left(\frac{r\sqrt{2}}{\omega_0}\right)^{|l|} \times L_p^{|l|}\left(\frac{2r^2}{\omega_0^2}\right) e^{-\frac{2r^2}{\omega_0^2}} e^{\mathrm{i}(2\pi I_l - nk_x x)} e^{-\mathrm{i}nl\theta} r\,\mathrm{d}r\,\mathrm{d}\theta. \quad (6)$$

The propagation term $\exp[\mathrm{i}(nk_x x + k_0 z)]$ dictates that the beam at the n-th diffraction order is associated with the topological number nl, and that when we monitor the beam traveling at an angle $\varphi = \arctan(k_x/k_0)$ to the zeroth-order direction, it possesses topological number l. The $p = 0$ component has the largest coefficient as it is the mode having the most overlap with the Gaussian beam. We thus generate a beam mostly consisting of LG_0^l at the first diffraction order [47]. When multiple LG beams with different topological charges l and the same beam waist are coaxially superimposed, they create interference patterns with characteristic intensity distributions. For two co-propagating LG beams with topological charges l_1 and l_2, the complex amplitude can be expressed as

$$\mathrm{LG}_0^{\{l_1,l_2\}} = \mathrm{LG}_0^{l_1} + \mathrm{LG}_0^{l_2}, \quad (7)$$

resulting in a pattern of $|l_2 - l_1|$ petals in the transverse intensity profile. The complex field distribution of multiplexed LG beams with unlimited integer topological charge numbers n at $z = 0$ can be written as

$$\mathrm{LG}_0 = \mathrm{LG}_0^{l_1} + \mathrm{LG}_0^{l_2} + \mathrm{LG}_0^{l_3} + \cdots + \mathrm{LG}_0^{l_\alpha}. \quad (8)$$

Each set of $\{l_1, l_2, l_3, \ldots, l_\alpha\}$ results in different characteristic petal-like intensity distributions with unique rotation directions contributed by the Gouy phase differences among the n superimposed OAM modes, leading to the unique patterns that are used for OAM demultiplexing through machine-learning-based image recognition schemes. For the experiment implementation, we uploaded the combined fork dislocation patterns with the desired OAM modes on the SLM1 to generate multiplexed OAM beams:

$$I_{\{l_1,l_2,\ldots l_\alpha\}} = \frac{1}{2} + \frac{1}{\alpha}\sum_{\alpha}\cos(k_x - l_\alpha\theta). \quad (9)$$

The output light then becomes

$$u_{\{l_1,l_2,\ldots,l_\alpha\}} = \sum_{p,n}\sum_{l=l_1}^{l_\alpha} U_{p,nl_\alpha}\mathrm{LG}_p^{nl_\alpha} e^{\mathrm{i}(nk_x x - k_0 z)}. \quad (10)$$

This is a multiplexed OAM beam containing components of l_1 to l_α, where U_{p,nl_α} is the coefficient of the $\mathrm{LG}_p^{nl_\alpha}$ component in the generated beam. Although we only intend to generate the $p = 0$ components, the $p > 0$ components still exist with relatively small coefficients compared to the $p = 0$ components. This causes a reduced energy efficiency, and clear side lobes, which are absent in standard LG beams.

B. Neural Network Architectures Computational Analysis

The total number of floating point operations (FLOPs) of our designed ECNN is calculated by

$$\mathrm{FLOPs}_{\mathrm{total}} = \mathrm{FLOPs}_{\mathrm{conv}} + \mathrm{FLOPs}_{\mathrm{ReLU}} + \mathrm{FLOPs}_{\mathrm{pooling}} + \mathrm{FLOPs}_{\mathrm{dense}}. \quad (11)$$

The FLOPs of the convolution layer $\mathrm{FLOPs}_{\mathrm{conv}}$ are calculated by the summation of multiplication operations:

$$\mathrm{conv}_{\mathrm{multiply}} = \mathrm{conv}_{h_i} \times \mathrm{conv}_{w_i} \times h_k \times w_k \times d \times n_k, \quad (12)$$

and addition operations:

$$\mathrm{conv}_{\mathrm{add}} = \mathrm{conv}_{h_i} \times \mathrm{conv}_{w_i} \times (h_k \times w_k - 1) \times n_k, \quad (13)$$

where h_i, w_i, h_k, and w_k are the height and width of input images and kernel, respectively. Then we have the total number of FLOPs for the convolution layer:

$$\mathrm{FLOPs}_{\mathrm{conv}} = \mathrm{conv}_{\mathrm{multiply}} + \mathrm{conv}_{\mathrm{add}}. \quad (14)$$

The FLOPs of the ReLU activation function layer $\mathrm{FLOPs}_{\mathrm{ReLU}}$ are calculated by

$$\mathrm{FLOPs}_{\mathrm{ReLU}} = \mathrm{conv}_{h_i} \times \mathrm{conv}_{w_i} \times n_k. \quad (15)$$

The FLOPs of the max pooling layer $\mathrm{FLOPs}_{\mathrm{pooling}}$ are calculated by

$$\mathrm{FLOPs}_{\mathrm{pooling}} = \mathrm{window} \times (\mathrm{window} - 1), \quad (16)$$

where the "window" is the number of pooling windows, calculated as

$$\text{window} = \frac{\text{conv}_{h_i}}{p} \times \frac{\text{conv}_{w_i}}{p} \times n_k. \tag{17}$$

The FLOPs of the dense layer $\text{FLOPs}_{\text{dense}}$ are calculated by the summation of the FLOPs of the first dense layer:

$$\text{FLOPs}_{d_1} = i_d \times n_1 + (i_d - 1) \times n_1, \tag{18}$$

and the FLOPs of the second dense layer:

$$\text{FLOPs}_{d_2} = n_1 \times n_2 + (n_1 - 1) \times n_2, \tag{19}$$

where i_d is the input dense neuron. The number of pooling windows (window) equals the number of input neurons to the dense layer (i_d) after the feature maps are flattened, as both represent the total number of features after the pooling operation. For the proposed PSNN, the total number of FLOPs $\text{FLOPs}_{\text{total}}$ is calculated by

$$\text{FLOPs}_{\text{total}} = \text{FLOPs}_{\text{optical}} + \text{FLOPs}_{\text{electronic}}. \tag{20}$$

The FLOPs for all optical components $\text{FLOPs}_{\text{optical}}$ in our designed Fourier phase shift layer are calculated by the summation of two-dimensional fast Fourier transform (2D FFT):

$$\text{FLOPs}_{\text{FFT}} = 5 \times H \times W \times \log_2(H \times W), \tag{21}$$

where H and W are the height and width of the input, and 5 is an empirical coefficient that accounts for the complex arithmetic operations required in practical FFT implementations, including the butterfly operations and complex number multiplications, which represents a conservative estimate of computational complexity, as the implementation efficiency may vary depending on hardware architecture. The phase extraction is

$$\text{FLOPs}_{\text{extraction}} = 11 \times H \times W, \tag{22}$$

where the factor of 11 represents the comprehensive count of elementary operations needed to extract the phase information from complex Fourier data. This includes operations for calculating the magnitude, computing the phase angle, and additional normalization operations required for practical implementations. Phase modulation with 16 phase masks is

$$\text{FLOPs}_{\text{pm}} = H \times W \times 16; \tag{23}$$

complex number reconstruction is

$$\text{FLOPs}_{\text{recons}} = 4 \times H \times W \times 16; \tag{24}$$

and inverse 2D FFT is

$$\text{FLOPs}_{\text{iFFT}} = 16 \times 5 \times H \times W \times \log_2(H \times W). \tag{25}$$

The total number of FLOPs in the optical component is

$$\text{FLOPs}_{\text{optical}} = \text{FLOPs}_{\text{FFT}} + \text{FLOPs}_{\text{ex}} + \text{FLOPs}_{\text{pm}} + \text{FLOPs}_{\text{recons}} + \text{FLOPs}_{\text{iFFT}}. \tag{26}$$

The total number of FLOPs of electronic layers is calculated by

$$\text{FLOPs}_{\text{electronic}} = \text{FLOPs}_{\text{pooling}} + \text{FLOPs}_{\text{ReLU}} + \text{FLOPs}_{\text{dense}}, \tag{27}$$

following the similar calculation configuration to ECNN.

We evaluate the energy efficiency of both ECNN and PSNN architectures in terms of operations per unit of power consumption. For the all-electronic ECNN, the energy efficiency is calculated by dividing the operational throughput by the total power consumption:

$$\text{GOPS/W}_{\text{ECNN}} = \frac{\text{FLOPs}_{\text{total}}}{T_{\text{ECNN}} \times P_{\text{electronic}}}, \tag{28}$$

where $\text{FLOPs}_{\text{total}}$ represents the total floating point operations per inference, T_{ECNN} is the processing time per epoch, and $P_{\text{electronic}}$ is the power consumption of the electronic components (225 W). This formulation captures the end-to-end computational efficiency of the electronic architecture. For the hybrid optical-electronic PSNN, the energy efficiency calculation accounts for both optical and electronic domains:

$$\text{GOPS/W}_{\text{PSNN}} = \frac{(\text{FLOPs}_{\text{optical}}/n_k) \times f}{P_{\text{optical}}} + \frac{\text{FLOPs}_{\text{electronic}}}{T_{\text{electronic}} \times P_{\text{electronic}}}, \tag{29}$$

where $\text{FLOPs}_{\text{optical}}$ represents operations performed in the optical domain, n_k is the number of phase kernels (16), f is the SLM refresh rate (60 Hz), P_{optical} is the power consumption of all optical components (273 W), $\text{FLOPs}_{\text{electronic}}$ represents operations performed electronically, $T_{\text{electronic}}$ is the processing time for electronic operation, and $P_{\text{electronic}}$ is the power consumption of the electronic component. The division of optical FLOPs by the number of phase kernels (n_k) accounts for the

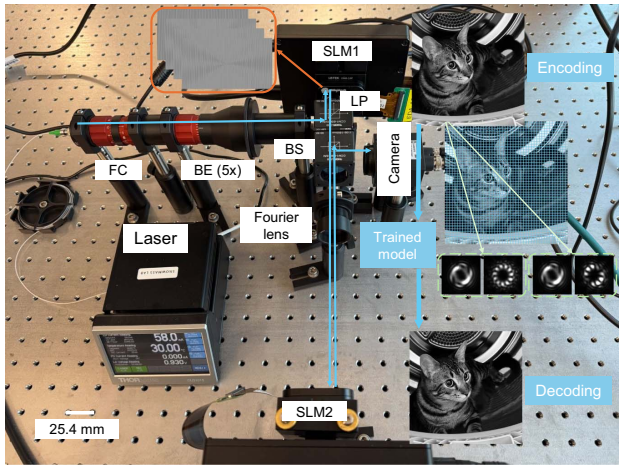

Fig. 7. Experimental implementation of the hybrid optical-electronic phase shift neural network (PSNN) building and image reconstruction using orbital angular momentum shift keying (OAM-SK) modulation over a 0.4 m free-space optical communication link. We use a Fabry–Perot laser diode with 1550 nm wavelength as the beam source. The collimated Gaussian-like beam is converted into the multiplexed OAM beams with desired modes using the spatial light modulator (SLM1), serving as the bit string being trained and used to encode the 8-bit grayscale image. The second SLM (SLM2) is placed at the back focal plane of a Fourier lens with focal length $f = 150$ mm, where the natural Fourier transform is passively completed and the feature extraction of the input beam is realized by phase modulation in the Fourier domain. The modulated output is inverse Fourier transformed and recorded as the electronic dataset sent to the electronic max-pooling layer and fully connected layers, completing the rest neural network training on computer electronically. FC: fiber coupler; BE: beam expander; BS: beam splitter; LP: linear polarizer. A scale bar of length 25.4 mm is drawn.

sequential processing nature of the SLM, which applies each phase mask individually. The optical power consumption encompasses the laser driver (10 W), two SLMs driven by laptops (2×130 W), and the camera (3 W), as the system configuration demonstrated in Fig. 7. The electronic power consumption represents the computational hardware required for the non-optical portions of the neural network.

Disclosures. The authors declare no conflicts of interest.

Data Availability. Data underlying the results presented in this paper are available from the corresponding author upon reasonable request.

REFERENCES

1. M. A. Khalighi and M. Uysal, "Survey on free space optical communication: a communication theory perspective," IEEE Commun. Surv. Tutor. **16**, 2231–2258 (2014).
2. Z. Ghassemlooy, W. Popoola, and S. Rajbhandari, *Optical Wireless Communications: System and Channel Modelling with MATLAB®* (CRC Press, 2019).
3. W. Yang, M. Wang, J. Zhang, *et al.*, "Narrowband wireless access for low-power massive internet of things: a bandwidth perspective," IEEE Wireless Commun. **24**, 138–145 (2017).
4. A. Goldsmith, *Wireless Communications* (Cambridge University Press, 2005).
5. H. Kaushal, V. Jain, and S. Kar, *Free Space Optical Communication* (Springer, 2017), Vol. **60**.
6. V. W. Chan, "Free-space optical communications," J. Lightwave Technol. **24**, 4750–4762 (2006).
7. H. Kaushal and G. Kaddoum, "Optical communication in space: challenges and mitigation techniques," IEEE Commun. Surv. Tutor. **19**, 57–96 (2016).
8. M. N. Sadiku, S. M. Musa, and S. R. Nelatury, "Free space optical communications: an overview," Eur. Sci. J. **12**, 55–68 (2016).
9. L. Allen, M. W. Beijersbergen, R. Spreeuw, *et al.*, "Orbital angular momentum of light and the transformation of Laguerre–Gaussian laser modes," Phys. Rev. A **45**, 8185 (1992).
10. G. Gibson, J. Courtial, M. J. Padgett, *et al.*, "Free-space information transfer using light beams carrying orbital angular momentum," Opt. Express **12**, 5448–5456 (2004).
11. J. Wang, J.-Y. Yang, I. M. Fazal, *et al.*, "Terabit free-space data transmission employing orbital angular momentum multiplexing," Nat. Photonics **6**, 488–496 (2012).
12. M. J. Padgett, "Orbital angular momentum 25 years on," Opt. Express **25**, 11265–11274 (2017).
13. M. Li, S. Yan, Y. Zhang, *et al.*, "Orbital angular momentum in optical manipulations," J. Opt. **24**, 114001 (2022).
14. K. Liu, Y. Cheng, Z. Yang, *et al.*, "Orbital-angular-momentum-based electromagnetic vortex imaging," IEEE Antennas Wirel. Propag. Lett. **14**, 711–714 (2014).
15. M. Krenn, R. Fickler, M. Fink, *et al.*, "Communication with spatially modulated light through turbulent air across Vienna," New J. Phys. **16**, 113028 (2014).
16. A. M. Yao and M. J. Padgett, "Orbital angular momentum: origins, behavior and applications," Adv. Opt. Photonics **3**, 161–204 (2011).
17. A. Mair, A. Vaziri, G. Weihs, *et al.*, "Entanglement of the orbital angular momentum states of photons," Nature **412**, 313–316 (2001).
18. R. Fickler, R. Lapkiewicz, M. Huber, *et al.*, "Interface between path and orbital angular momentum entanglement for high-dimensional photonic quantum information," Nat. Commun. **5**, 4502 (2014).
19. E. Nagali, F. Sciarrino, F. De Martini, *et al.*, "Quantum information transfer from spin to orbital angular momentum of photons," Phys. Rev. Lett. **103**, 013601 (2009).
20. A. Nicolas, L. Veissier, L. Giner, *et al.*, "A quantum memory for orbital angular momentum photonic qubits," Nat. Photonics **8**, 234–238 (2014).
21. T. Stav, A. Faerman, E. Maguid, *et al.*, "Quantum entanglement of the spin and orbital angular momentum of photons using metamaterials," Science **361**, 1101–1104 (2018).
22. M. Ritsch-Marte, "Orbital angular momentum light in microscopy," Philos. Trans. R Soc. A: Math. Phys. Eng. Sci. **375**, 20150437 (2017).
23. L. Clark, A. Béché, G. Guzzinati, *et al.*, "Quantitative measurement of orbital angular momentum in electron microscopy," Phys. Rev. A **89**, 053818 (2014).
24. B. J. McMorran, A. Agrawal, P. A. Ercius, *et al.*, "Origins and demonstrations of electrons with orbital angular momentum," Philos. Trans. R Soc. A: Math. Phys. Eng. Sci. **375**, 20150434 (2017).
25. J. Leach, M. J. Padgett, S. M. Barnett, *et al.*, "Measuring the orbital angular momentum of a single photon," Phys. Rev. Lett. **88**, 257901 (2002).
26. G. C. Berkhout, M. P. Lavery, J. Courtial, *et al.*, "Efficient sorting of orbital angular momentum states of light," Phys. Rev. Lett. **105**, 153601 (2010).
27. M. P. Lavery, D. J. Robertson, G. C. Berkhout, *et al.*, "Refractive elements for the measurement of the orbital angular momentum of a single photon," Opt. Express **20**, 2110–2115 (2012).
28. S. Pachava, R. Dharmavarapu, A. Vijayakumar, *et al.*, "Generation and decomposition of scalar and vector modes carrying orbital angular momentum: a review," Opt. Eng. **59**, 041205 (2020).
29. Y. Ren, G. Xie, H. Huang, *et al.*, "Adaptive-optics-based simultaneous pre-and post-turbulence compensation of multiple orbital-angular-momentum beams in a bidirectional free-space optical link," Optica **1**, 376–382 (2014).
30. T. Doster and A. T. Watnik, "Machine learning approach to oam beam demultiplexing via convolutional neural networks," Appl. Opt. **56**, 3386–3396 (2017).
31. F. Feng, J. Hu, Z. Guo, *et al.*, "Deep learning-enabled orbital angular momentum-based information encryption transmission," ACS Photonics **9**, 820–829 (2022).
32. J. Li, M. Zhang, and D. Wang, "Adaptive demodulator using machine learning for orbital angular momentum shift keying," IEEE Photonics Technol. Lett. **29**, 1455–1458 (2017).
33. X. Cui, X. Yin, H. Chang, *et al.*, "Experimental study of machine-learning-based orbital angular momentum shift keying decoders in optical underwater channels," Opt. Commun. **452**, 116–123 (2019).
34. J. Liu, P. Wang, X. Zhang, *et al.*, "Deep learning based atmospheric turbulence compensation for orbital angular momentum beam distortion and communication," Opt. Express **27**, 16671–16688 (2019).
35. E. Knutson, S. Lohani, O. Danaci, *et al.*, "Deep learning as a tool to distinguish between high orbital angular momentum optical modes," Proc. SPIE **9970**, 997013 (2016).
36. R. Sun, L. Guo, M. Cheng, *et al.*, "Identifying orbital angular momentum modes in turbulence with high accuracy via machine learning," J. Opt. **21**, 075703 (2019).
37. H. Li, A. Kadav, I. Durdanovic, *et al.*, "Pruning filters for efficient convnets," arXiv, arXiv:1608.08710 (2016).
38. D. Psaltis and N. Farhat, "Optical information processing based on an associative-memory model of neural nets with thresholding and feedback," Opt. Lett. **10**, 98–100 (1985).
39. P. Gupta and S. Li, "4F optical neural network acceleration: an architecture perspective," Proc. SPIE **12019**, 120190B (2022).
40. Y. Chen, "4F-type optical system for matrix multiplication," Opt. Eng. **32**, 77–79 (1993).
41. L. Fan, X. Long, J. Dai, *et al.*, "Optical–electronic hybrid Fourier convolutional neural network based on super-pixel complex-valued modulation," Appl. Opt. **62**, 1337–1344 (2023).
42. M. Born and E. Wolf, *Principles of Optics: Electromagnetic Theory of Propagation, Interference and Diffraction of Light*, 7th ed. (Cambridge University Press, 1999).
43. M. Mirhosseini, M. Malik, Z. Shi, *et al.*, "Efficient separation of the orbital angular momentum eigenstates of light," Nat. Commun. **4**, 2781 (2013).

44. H. Luan, D. Lin, K. Li, *et al.*, "768-ary Laguerre–Gaussian-mode shift keying free-space optical communication based on convolutional neural networks," Opt. Express **29**, 19807–19818 (2021).
45. Z. Liu, S. Yan, H. Liu, *et al.*, "Superhigh-resolution recognition of optical vortex modes assisted by a deep-learning method," Phys. Rev. Lett. **123**, 183902 (2019).
46. G. Vallone, "On the properties of circular beams: normalization, laguerre–gauss expansion, and free-space divergence," Opt. Lett. **40**, 1717–1720 (2015).
47. B. Sephton, A. Dudley, and A. Forbes, "Revealing the radial modes in vortex beams," Appl. Opt. **55**, 7830–7835 (2016).